SUPPLEMENTAL INFORMATION

This files contains supplemental methods, supplemental references, 3 supplemental tables, 7 supplemental figures and figure legends.

SUPPLEMENTAL METHODS

Imaging set-ups:

Live-cell imaging was performed on two different inverted spinning-disk confocal microscopes equipped with motorized stages, automatic focus and controlled with MetaMorph® (Microscopy Automation & Image Analysis Software). The first one (Nikon Ti-Eclipse), is equipped with a Yokogawa CSU-X1FW spinning head, and an EM-CCD camera (Hamamatsu), a 100× oil-immersion objective (Nikon CFI Plan Apo DM 100×/1.4 NA) and a 2.5× magnifying lens, yielding a pixel size of 43nm. The second one (Leica DMI8), is equipped with a Yokogawa CSU-W1 spinning head, and a sCMOS Orca-Flash 4 V2+ (Hamamatsu) a 100× oil-immersion objective (Leica Plan Apo DM 100×oil/1.4 NA), yielding a pixel size of 70nm.

The laser ablation set up uses a pulsed 355 nm ultraviolet laser interfaced with an iLas system (Roper Scientific) in the ‘‘Mosquito’’ mode. This allows irradiating at multiple positions in the field with laser spots. This system was mounted on the Nikon confocal spinning disk, using a 60x oil-immersion objective (CFI Apochromat 60x Oil λS, 1.4 NA, Nikon) in combination with a 2.5x magnifying lens. The irradiation was performed with a low laser power, in order to minimize bleaching of the lectin labeling. The irradiation was repeated 3-5 times, until the cell visibly deflated with a clear ejection of cytosolic material observable in bright field, to ensure complete wall relaxation. Cells were imaged before and immediately after ablation, switching to a 100× oil-immersion objective (Nikon CFI Plan Apo DM 100×/1.4 NA) and a 2.5× magnifying lens. The full process, including the first image acquisition, laser ablation and the second image after ablation, was typically performed in less than 2 minutes.

Image analysis:

Cell Wall thickness computation: Wall thickness measurement was performed as in (1), including chromatic shift registration and correction. Images of cells labeled for the plasma membrane (GFP-Psy1) and cell wall surface (*Gs*-IB$_4$-Alexafluor647) were analyzed. For measurement in other fission yeasts, the membrane labelling was achieved by using FM4-64 (Invitrogen). For this, cells were incubated for 10 min in the dye at a final concentration of

www.pnas.org/cgi/doi/10.1073/pnas.1820455116

5µg/ml from a 100X stock in DMSO. This provided sharp membrane labelling on cell sides, but did not allow to map thickness at cell tips. From those signals, a first binarization defined the most external cell boundary, on which perpendicular lines were defined at each pixel. Because some of the mutants showed a variable intracellular background, plausibly due to partial defects in Psy1 delivery to plasma membrane or increased auto-fluorescence, we systematically implemented a correction script to extract the true signal peak by using an analytical expression of the convoluted intensity profile (1, 2).

Cell Shape and local Cell Wall thickness measurements: For each cell, wall boundaries were obtained by binarization of mid-slice confocal fluorescent images of lectin-Alexafluor647 label, before and after laser ablation. For some cells, the results were manually updated, to correct for local signal bleaching after laser ablation. The long axis of the cell was automatically detected and used to define cell length. Old and new ends were defined by the user, and local radii of curvature ($R_{c1\text{-}0}$) were measured by fitting local tips with a circle using a portion of the cell surface of 3.44 µm around the center of the tip; the same section was used to measure tip wall thickness. The two scar bulges localization was defined by the user, scar radius was automatically measured as the distance between them, and thickness computed as a mean of values on a distance of 0.430 µm around the selected center. Cell sides limits (single or multiple) were defined by the user, and the radius of the cell ($R_{1\text{-}0}$) was measured as the mean of all diameters on the selected region, as well as side thickness. Birth scars were sometimes superimposed on the selected side region, like in multi-scarred cells. In such cases, the scar region (0.430 µm around the selected center) was automatically excluded to compute side parameters. Those geometrical features were fed into analytical expressions reported in methods, or 3D simulations (see below) to extract elastic moduli.

A full package including all relevant information, scripts and examples to implement those methods is available on our research web page: http://www.minclab.fr/research

GFP-Bgs4 concentration measurements: To analyze the localization of polar factors we used the same approach as in (1). Cells expressing GFP-Bgs4 were labeled with *Gs*-IB_4-Alexafluor647. The cell was first segmented by using the signal from the lectin-labelled cell wall, in order to extract the whole-cell contour. Fluorescent signals of interest were then extracted from fluorescent images by using a mask based on corresponding sub-regions. Signals were corrected for the background signal:

$$I_{tip} = I_{tip\,raw} - I_{bg}$$
$$I_{cell\ contour} = I_{cell\ contour\ raw} - I_{bg}$$

The polarization index (PI) was defined as the ratio between the mean intensity of the two tips divided by the intensity along the whole cell contour, as in (3):

$$PI = \frac{I_{tip}}{I_{cell\ contour}}$$

3D cell reconstruction: To analyze cell shapes in microchannel experiments, z-stacks of the membrane label GFP-Psy1 covering the whole depth of the cell were acquired with a z-step of 200 nm. Images were segmented using the Limeseg plugin for Fiji (4), which converts the stack into a 3D surface mesh. This reconstructed cell shape was analyzed using a custom Matlab script available online at https://github.com/SergeDmi/analyze_pombe. A closed curve was fitted to the points of the central slice using a spline-fitting tool adapted from (5); the perimeter was determined as the length of this curve.

Osmotic treatments:

Estimation of relative values of turgor pressure: To estimate pressure values, cells grown in YE5S and pre-labeled with 5 mg/ml *Gs*-IB_4 -Alexafluor647 were placed in homemade glass channels, imaged, and subsequently rinsed with YE5S+5 mg/ml *Gs*-IB_4 -Alexafluor647 supplemented with different doses of sorbitol and imaged again less than 5 minutes after treatment. Turgor pressure was computed as previously described in (6). The external osmolarity at which the cell wall reaches its relaxed state was estimated from a comparison with laser ablation data, considering this last as the fully relaxed wall state (Fig. S3G). The same values for sorbitol, glycerol and YE osmolarity, molarity to molality conversion coefficients, and cell inaccessible volume fractions were used as in (6). Volumes before (V_1) and after (V_0) ablation were measured at the population of each mutant, considering the central part of the cell as a cylinder and the two ends as hemispheres. The analysis of shape changes during osmotic treatments, were computed from the lectin signal using ImageJ. The diameter was calculated as an average of 5 measurements along the cylindrical part of the cell.

Dynamic hyper and hypo-osmotic shocks: Cells grown in YE5S were harvested, washed once in YE5S+1M sorbitol, and incubated in the same media for more than 45-60 min for adaptation.

This timing was set from a time-course calibration for diameter and growth recovery upon sorbitol treatment, which suggested full turgor recovery after ~ 60min. Longer adaptations were also assessed and did not alter the differential response reported in Figure 4H. 10 mg/ml *Gs*-IB_4 -Alexafluor647 was added to the cells during 10 min, and cells were subsequently placed into separate homemade glass channels filled with YE5S+10 mg/ml *Gs*-IB_4 -Alexafluor647, imaged and rinsed with YE5S for hypoosmotic treatment or with YE5S+2M sorbitol for hyperosmotic treatment. For the experiment with YE5S+0.5M sorbitol (Fig. S7E-S7G), adaptation was also done for at least 60min, and cells were then rinsed in either YE5S for hypoosmotic treatment or with YE5S+1M sorbitol for hyperosmotic treatment. For treatment with YE5S+1.5M sorbitol (Fig. S7E-S7F), adaptation was done for at least 120 min, and cells were then rinsed in either YE5S for hypoosmotic treatment or with YE5S+3M sorbitol for hyperosmotic treatment. Cells were imaged again less than 3 minutes after treatment. Expansion and deflation were mostly homogenous along the cells sides, with no notable local changes close to cell tips. The quantification of diameter changes was achieved by computing the diameters at 5 different position along the cell sides.

Simulation methods to compute elastic moduli:

The analytical formula mentioned in methods were validated at the cylindrical sides and at hemispherical tips with the numerical resolution of the partial differential equations governing thin elastic shells (7) (Fig. S1C-S1L). When local cell shapes were not perfectly cylindrical, for instance to analyze bulk moduli at birth scars (Fig. 1D), we derived values for the bulk modulus using this computational approach only. Those simulations were further used to confirm experimental estimations based on analytical expressions in cells with varying diameters (Fig. S3B-S3F) and in skittle-like cells (Fig. S5E), and yielded near-exact values for rod and rod-like parts of the cells.

The estimation procedure of cell mechanical parameters is achieved using a 3D simulation based on theory of elasticity, as detailed in the supplementary text of (7). For this, we consider the partial differential equations governing axisymmetric thin elastic shells, assuming that the Poisson ratio is 0 and that bending stiffness is negligible, and we solve them numerically. Thanks to the axisymmetric shape of the fission yeast cell wall envelope, the 2D mechanical problem of the whole surface can be reduced to a 1D numerical problem. The equation proposed by Su and Taber (8) for pressurized axisymmetric thin shell was solved to calculate the

deformation of the axisymmetric shell approximating the yeast cell wall. The boundary conditions are that the two curvatures (κ_{11} and κ_{22}) and the two deformations (λ_{11} and λ_{22}) are equal on the two points laying on the axis of rotational symmetry, while the transverse shear Q_2 is 0 at those points. Details on the numerical methods and their validations are available in (7, 9). The system of equations reads:

$$\partial_s r = \lambda_{22}\cos(\phi) + \gamma_2 \sin(\phi) \quad (1)$$

$$\partial_s z = \lambda_{22}\sin(\phi) - \gamma_2 \cos(\phi) \quad (2)$$

$$\partial_s \phi = \alpha(\kappa_{22} + \partial_s \phi_0) \quad (3)$$

$$\partial_s V_{2b} = -r\alpha p_v \quad (4)$$

$$\partial_s H_{2b} = \alpha\left(\frac{\partial w}{\partial \lambda_{11}} - r p_h\right) \quad (5)$$

$$\partial_s M_{22b} = \alpha\left(\cos(\phi)\frac{\partial w}{\partial \kappa_{11}} + r Q_2 \lambda_{22} - r H_2 \gamma_2\right) \quad (6)$$

With:

r, z = radial and azimuthal coordinates of the axisymmetric contour.

ϕ, ϕ_0 = meridional angles after and before deformation.

ii=11, 22, meridional versus longitudinal direction.

λ_{ii}= Deformation along ii.

γ_2 corresponds to the transverse shear deformation.

κ_{ii} = Difference between rest state curvature and swelled state curvature along ii.

Γs corresponds to the shear angle.

N_{ii} = Stresses along ii.

N_{22} is decomposed between a vertical component V_2 and a horizontal component H_2.

Q_2 = transverse shear stress.

M_{ii} = bending moment.

p = Turgor pressure, w= elastic energy, Y= Young modulus, v=Poisson ratio.

Other variables are used for numerical purposes (H_{2b}, V_{2b}, M_{22b}, α). They all are linked by the following relationships:

$$H_2 = \frac{H_{2b}}{r}\ ,\ \ M_{22} = \frac{M_{22b}}{r}, H_2 = \frac{V_{2b}}{r} \tag{7-9}$$

$$N_{22} = H_2\cos(\phi) + V_2\sin(\phi),\ \ Q_2 = H_2\sin(\phi) - V_2\cos(\phi) \tag{10-12}$$

$$\lambda_{11} = \frac{r}{r_0}\ , \kappa_{11} = \frac{\sin(\phi)}{r} - \frac{\sin(\phi_0)}{r_0}, \alpha = \sqrt{\gamma_2^2 + \lambda_{22}^2} \tag{13-15}$$

$$\Gamma_s = \arctan\left(\frac{\gamma_2}{\lambda_{22}}\right), p_h = p\ sin(\phi - \Gamma_s), p_v = -p\ cos(\phi - \Gamma_s) \tag{16-18}$$

The following linear elastic energy including both transverse shear and bending was sufficient to describe wall relaxation experiments from laser ablation:

$$w(\lambda_{11}, \lambda_{22,}\gamma_2, \kappa_{11,}\kappa_{22}) = A((\lambda_{11} - 1)^2 + 2\nu(\lambda_{11} - 1)(\lambda_{22} - 1) + (\lambda_{11} - 1)^2) + B\gamma_2^2 + C({\kappa_{11}}^2 + 2\upsilon\kappa_{11}\kappa_{22} + {\kappa_{22}}^2) \tag{19}$$

with, $A = \frac{Yh}{2(1-\nu^2)}$, B= $\frac{Yh}{4(1+\nu)}$, C=$\frac{Yh^3}{24(1-\nu^2)}$. (20-22)

The system of ODE was closed by the three following algebraic equations which involve the variables λ_{22}, κ_{22}, γ_2 :

$$\lambda_{22} = (1 + \frac{N_{22}}{2A} - \nu(\lambda_{11} - 1)) \tag{23}$$

$$\gamma_2 = \frac{Q_2}{2B} \tag{24}$$

$$\kappa_{22} = \frac{M_{22}}{2C} - \nu\kappa_{11} \tag{25}$$

The following procedure was thus implemented, using the numerical procedure described in (7): The relaxed contour of the cell was swollen by computing the stress pattern from the curvatures, and elastic strain from stress, with an internal pressure of 1MPa, supposing a one-parameter family of Young-modulus distributions (see below), the best fitting parameter for the turgid contour was retained to calculate the estimate. The chosen one-parameter families of Young modulus distributions are the following:

- For the estimation of the scar modulus in Figure 1D, we used a distribution of Young's modulus along the curvilinear abscissa x (The 0 of the curvilinear abscissa being taken at the oe and the abscissa being expressed in μm), defined by the formula:

$$Y(x) = (Y_{oe} + ((Y_{side} - Y_{oe}) * (\text{sigmoid}(x, (x_{oe} + w_{tip} + x_{side\_center})/2,\ 5/(x_{side\_centre}/2 - x_{oe} - w_{tip})))) + ((Y_{scar} - Y_{side}) * (\text{sigmoid}(x, (x_{scar} - w_{scar} + x_{side\_centre})/2,\ 10/(x_{side\_centre} - x_{scar} - w_{scar})))) + ((Y_{ne} - Y_{scar}) * (\text{sigmoid}(x, (x_{scar} + w_{scar} + x_{ne} - w_{tip})/2,\ 5/(x_{ne} - w_{tip} - x_{scar} - w_{scar}))))) \quad (26)$$

The subscript oe, ne, scar, tip, side_centre correspond to the curvilinear abscissa x at the middle of the old end (oe) , the middle of the new end (ne), the middle of the scar (scar), the middle of the cell side (side); and w_{tip} = 1.7 µm corresponds to the tip half curvilinear length and w_{scar} = 0.21 µm corresponds to the scar half curvilinear length. This formula allows to generate a smooth profile of young's moduli and connect the different part of the cell (new end, old end, sides and scars). The sigmoid function is defined by:

$$\text{sigmoid}(x, c, a) = \frac{1}{1 + \exp(-a(x - c))}$$

Y_{oe}, Y_{side}, Y_{ne} are estimated independently using analytical formula for spherical, and cylindrical pressure vessel; Y_{scar} is the sole free-parameter.

- In Figure S1K, the side modulus is estimated by running simulations with: $Y(x) = Y_{side}$. The $Y_{sidesim}/P$ estimated through simulations is 1.07±0.025 (N=27) times smaller than Y_{side}/P estimated using the analytical formula for a cylindrical pressure vessel.

- In Figure S1K, the oe and ne moduli are estimated by running simulations with the following Young modulus distribution:

$$Y(x) = (Y_{oesim} + ((Y_{side} - Y_{oesim}) * (\text{sigmoid}(x, (x_{oe} + w_{tip} + x_{side\_center})/2,\ 5/(x_{side\_center}/2 - x_{oe} - w_{tip})))) + ((Ynesim - Yside) * (\text{sigmoid}(x, (x_{ne} + w_{tip} + x_{side\_center})/2,\ 10/(x_{ne} - w_{tip} - x_{side\_center}))))). \quad (27)$$

$Y_{oesim}=(1-t)*Y_{oe}+t*Y_{side}$, $Y_{nesim}=(1-t)*Y_{ne}+t*Y_{side}$. Y_{oe}, Y_{side}, Y_{ne} are estimated independently using analytical formula for spherical, and cylindrical pressure vessel. For each cell, the best fitting parameter t is retained to estimate Y_{oesim} and Y_{nesim}. The estimation for t is: 0.3704±0.13 (N=27), with w_{tip} = 1.7 µm and w_{scar} = 0.21 µm as above.

The distribution of Young moduli in the central zone of the cell in Figure S5E is calculated using the thickness profile and the diameter of the cell through the formula of the linear

regressions from Figure 3B for *myo1Δ* and *ubr1Δ* supposing P=1MPa. The distributions are connected at both tips to the analytical estimations of the moduli by fitting a second order polynomial function between the cell wall portion closest from the tip and the tip itself. For *myo1Δ*, the simulated swelling in Figure S5E corresponds to P=1MPa and for *ubr1Δ*, the simulated swelling corresponds to P=1.3MPa (the Young modulus estimated in Figure 3B was found to be slightly too high).

The estimated mechanical parameters for the cells represented figure S1K and figure S3C are listed below:

strain	Y_{cyl} (MPa)	Y_{OE} (MPa)	Y_{NE} (MPa)	Y_{scar} (MPa)
WT	49	23	27	49
dad1Δ	31	36	36	55
myo1Δ	46	37	68	56
ubr1Δ	37	29	26	40
scd2Δ	38	26	61	42

Table S1: Mechanical parameters for simulations of cells presented in Figures S1K and S3C.

Range of validity of the analytical approximations to infer elastic moduli

Axisymmetric thin shells mimicking the relaxed *S. pombe* cells by a cylinder enclosed by two semi-ellipsoids at the tip with physiological parameters (h_s= 0.2 μm, R_0=2 μm, Poisson ratio ν=0, and Y_s/P = 40) were numerically swollen to systematically test the validity range of the analytical formula presented in Material and Methods of the main text:

- In a first set of simulations, the cylinder length was varied from 0 to 40 μm while keeping the tips hemispherical (Fig. S1C). The analytical prediction of the radial and longitudinal deformations, which are equal at the tip ($\lambda_{tip} = Rc/Rc_0=1/(1-PR_0/(2Y_{tip}h_s))$), has an accuracy that is always better than 1% (Fig. S1E). The radial deformation at the center of the cylinder is predicted by the analytical formula ($\lambda_{r,cyl}= R_1/ R_0=1/(1-PR_0/(Y_{side}h_s))$) with 10% accuracy if $L_0/R_0>2$, 1% accuracy if $L_0/R_0>4$, and 0.1% for $L_0/R_0>5$ (Fig. S1F). Given the experimental range of WT, mutants and cells from other fission species (Fig. S1F), we conclude that the effect of finite

cylinder length on the accuracy of the analytical formula is expected to be better than 5% for all cells considered here.

- In a second set of simulations, the cylinder length and radius were kept constant at 10 μm and 2 μm respectively, while varying the tip ellipticity (Fig. S1D). The deformation in the cylindrical part is not affected by the tip shape (Fig. S1H) while the deformation at the tip diverges from the analytical prediction when the ellipticity diverges from that of a sphere (the radius R_0 in the analytical formula is obtained by fitting a circle on the elliptical shape of the tip) (Fig. S1G). Therefore, tip shape has virtually no effect on the side modulus inferred from the analytical formula. Measurement of ellipticity of a representative set of cells used in this study show that relaxed tips are nearly spherical, with average values of R_t/R_0 close to 1 and always between 0.8 and 1.2, implying that the error on tip modulus due to ellipticity is generally small and at most around 40%.

- In a third set of simulations, the cylinder length and radius were kept constant at 10 μm and 2 μm respectively, the tips were kept hemispherical, while the tip Young modulus was varied (Fig. S1I-J). The error in the prediction of the tip deformation remains below 5 % when the tip Young modulus is greater than half of the side Young modulus (Fig. S1I), which applies to all cells considered here. The analytical prediction of the deformation in the cylindrical part are not affected by the Young modulus at the tip (Fig. S1J). Therefore the effect of local wall elasticity on the accuracy of the analytical formula is expected to be better than 5% for all cells considered here.

- In a last set of simulations, Y_{side}/P was varied (Fig. S7D). For $Y_s/P = 40$, the cylindrical part remains cylindrical while it becomes slightly ovalized for $Y_s/P = 20$. This indicates that non-linear geometric effects increase deformations at higher pressure and so cannot account for strain-stiffening as observed in our experiments (Fig. 4G-4H).

SUPPLEMENTAL REFERENCES:

1. Davì V, *et al.* (2018) Mechanosensation Dynamically Coordinates Polar Growth and Cell Wall Assembly to Promote Cell Survival. *Developmental Cell* 45(2):170-182.e177.
2. Clark AG, Dierkes K, & Paluch EK (2013) Monitoring actin cortex thickness in live cells. *Biophys J* 105(3):570-580.
3. Haupt A, Ershov D, & Minc N (2018) A Positive Feedback between Growth and Polarity Provides Directional Persistency and Flexibility to the Process of Tip Growth. *Curr Biol* 28(20):3342-3351 e3343.
4. Machado S, Mercier V, & Chiaruttini N (2018) LimeSeg: A coarsed-grained lipid membrane simulation for 3D image segmentation. *bioRxiv*.
5. Mathur A, *et al.* (2018) Cytoskeleton mechanics determine resting size and activation dynamics of platelets. *bioRxiv*.
6. Atilgan E, Magidson V, Khodjakov A, & Chang F (2015) Morphogenesis of the Fission Yeast Cell through Cell Wall Expansion. *Curr Biol* 25(16):2150-2157.
7. Abenza JF, *et al.* (2015) Wall mechanics and exocytosis define the shape of growth domains in fission yeast. *Nat Commun* 6:8400.
8. Su F-C & Taber LA (1992) Torsional boundary layer effects in shells of revolution undergoing large axisymmetric deformation. *Computational Mechanics* 10(1):23-37.
9. Kempski MH, Taber LA, & Su F-C (1988) Large Elastic Deformation of Shear Deformable Shells of Revolution: Numerical and Experimental Results. *Journal of Applied Mechanics* 55(3):629-634.

Gene ID	GO biological processes					
scd2	signaling	establishment or maintenance of cell polarity	conjugation with cellular fusion			
myo52	mitotic cytokinesis	actin cytoskeleton organization	establishment or maintenance of cell polarity			
coq10	cofactor metabolic process					
kin1	mitotic cytokinesis	membrane organization	actin cytoskeleton organization	establishment or maintenance of cell polarity		
pub1	protein catabolic process	transmembrane transport	protein modification by small protein conjugation or removal			
mae2	generation of precursor metabolites and energy					
vps1	peroxisome organization	membrane organization	vesicle-mediated transport			
dad1	meiotic nuclear division	mitotic sister chromatid segregation				
yaf9	DNA repair	regulation of transcription, DNA-templated	chromatin organization	transcription, DNA-templated		
plc1	signaling	lipid metabolic process				
gpa1	ascospore formation	signaling	conjugation with cellular fusion			
myo1	membrane organization	protein-containing complex assembly	actin cytoskeleton organization	vesicle-mediated transport	establishment or maintenance of cell polarity	
efc25	signaling	establishment or maintenance of cell polarity				
ubr1	signaling	protein catabolic process	regulation of transcription, DNA-templated	protein modification by small protein conjugation or removal	transcription, DNA-templated	
rdp1	regulation of transcription, DNA-templated	meiotic nuclear division	chromatin organization	transcription, DNA-templated		
rga2	signaling					
rga4	signaling	actin cytoskeleton organization	establishment or maintenance of cell polarity			
mtq2	cytoplasmic translation					
wsc1	signaling					
mtl2	signaling					
rgf2	cell wall organization or biogenesis	signaling				
rgf1	signaling	carbohydrate metabolic process	cell wall organization or biogenesis			
pmk1	metal ion homeostasis	signaling	transmembrane transport	regulation of transcription, DNA-templated	transcription, DNA-templated	cell wall organization or biogenesis
pck2	signaling	carbohydrate metabolic process	establishment or maintenance of cell polarity	cell wall organization or biogenesis		
agn1	carbohydrate metabolic process	conjugation with cellular fusion	cell wall organization or biogenesis			
omg1	carbohydrate metabolic process	conjugation with cellular fusion	cell wall organization or biogenesis			

Table S2: Gene functions for the set of mutants used in Figure 2, assigned from the Gene Ontology classification (https://www.pombase.org/).

h+ *GFP-psy1:ade bgs4::ura4 RFP-bgs4-Leu* (*leu1-32 ura4-D18 ade6*)	This study	VD57
h- *GFP-psy1:ade bgs4::ura4 RFP-bgs4-Leu* (*leu1-32 ura4-D18 ade6*)	This study	VD58
h+ *bgs4::ura4 RFP-bgs4-Leu* (*leu1-32 ura4-D18 ade6-M216*)	This study	NM387
h- *rga2::KanMX bgs4::ura4 RFP-bgs4-Leu GFP-psy1:ade* (*leu1-32 ura4-D18*)	This study	VD72
h- *rga4::KanMX bgs4::ura4 RFP-bgs4-Leu GFP-psy1:ade* (*leu1-32 ura4-D18*)	This study	VD81
h+ wsc1::KanMX GFP-psy1:ade bgs4::ura4 RFP-bgs4:leu (*leu1-32 ura4-D18 ade6*)	This study	VD158
h- *mtl2::KanMX GFP-psy1:ade bgs4::ura4 RFP-bgs4:leu* (*leu1-32 ura4-D18 ade6*)	This study	VD160
h- *pck2::leu GFP-psy1:ade*	This study	VD109
h+ *rgf2::ura GFP-psy1:ade* (*leu1-32 ura4-D18 ade6*)	This study	VD164
h+ *rgf1::KanMX GFP-psy1:ade* (*leu1-32 ura4-D18 ade6*)	This study	VD167
h+ *pmk1:ura GFP-psy1:leu* (*leu1-32 ura4-D18*)	This study	VD173
h+ *scd2::KanMX CRIB-tdTomato:ura Leu:GFP-psy1 (ura4-D18 leu1-32)*	This study	VD97
h+ *myo52::ura CRIB-tdTomato:ura Leu:GFP-psy1 (ura4-D18 leu1-32)*	This study	VD127
h+ *coq10::KanMX GFP-psy1:ade (ade6-M216 ura4-D18 leu1-32)*	This study	HG77*
h+ *kin1::KanMX GFP-psy1:ade (ade6-M216 ura4-D18 leu1-32)*	This study	HG101*
h+ *pub1::KanMX GFP-psy1:ade (ade6-M216 ura4-D18 leu1-32)*	This study	HG72*
h+ *mae2::KanMX GFP-psy1:ade (ade6-M216 ura4-D18 leu1-32)*	This study	HG74*
h+ *vps1::KanMX GFP-psy1:ade (ade6-M216 ura4-D18 leu1-32)*	This study	HG31*
h+ *dad1::KanMX GFP-psy1:ade (ade6-M216 ura4-D18 leu1-32)*	This study	HG76*
h+ *yaf9::KanMX GFP-psy1:ade (ade6-M216 ura4-D18 leu1-32)*	This study	HG103*
h+ *plc1::KanMX GFP-psy1:ade (ade6-M216 ura4-D18 leu1-32)*	This study	HG104*
h+ *gpa1::KanMX GFP-psy1:ade (ade6-M216 ura4-D18 leu1-32)*	This study	HG106*
h+ *myo1::KanMX: GFP-psy1:ade (ade6-M216 ura4-D18 leu1-32)*	This study	HG27*
h+ *efc25::KanMX GFP-psy1:ade (ade6-M216 ura4-D18 leu1-32)*	This study	HG29*
h+ *ubr1::KanMX GFP-psy1:ade (ade6-M216 ura4-D18 leu1-32)*	This study	HG33*
h+ *rdp1::KanMX GFP-psy1:ade (ade6-M216 ura4-D18 leu1-32)*	This study	HG35*
h+ *mtq2::KanMX GFP-psy1:ade (ade6-M216 ura4-D18 leu1-32)*	This study	HG116*
h+ *agn1:KanMX GFP-psy1:ade (ade6-M216 ura4-D18 leu1-32)*	This study	HG75*
h+ *omg1:KanMX GFP-psy1:ade (ade6-M216 ura4-D18 leu1-32)*	This study	HG121*
h90 rga4::KanMX ade6<<GFP-psy1 bgs4::ura4 RFP-bgs4-Leu	This study	VD162
h+ msy2::KanMX *(ade6-M216 ura4-D18 leu1-32)*	This study	AH 233*
h- msy1::ura4 msy2::KanMX *(ade6-M216 ura4-D18 leu1-32)*	H. Lida	NM 516
Schizosaccharomyces japonicus, wild-type, homothallic	YGRC	VD210
Schizosaccharomyces octosporus, wild-type, homothallic	YGRC	VD211
Schizosaccharomyces cryophilus, wild-type, homothallic	N. Rhind	VD212

Table S3. Yeast strains used in this study. * Strains derived from the commercially available '*S. pombe* Haploid Deletion Mutant Set version 2.0' strains collection (Bioneer Corporation; http://pombe.bioneer.com).

FIGURES AND FIGURE LEGENDS

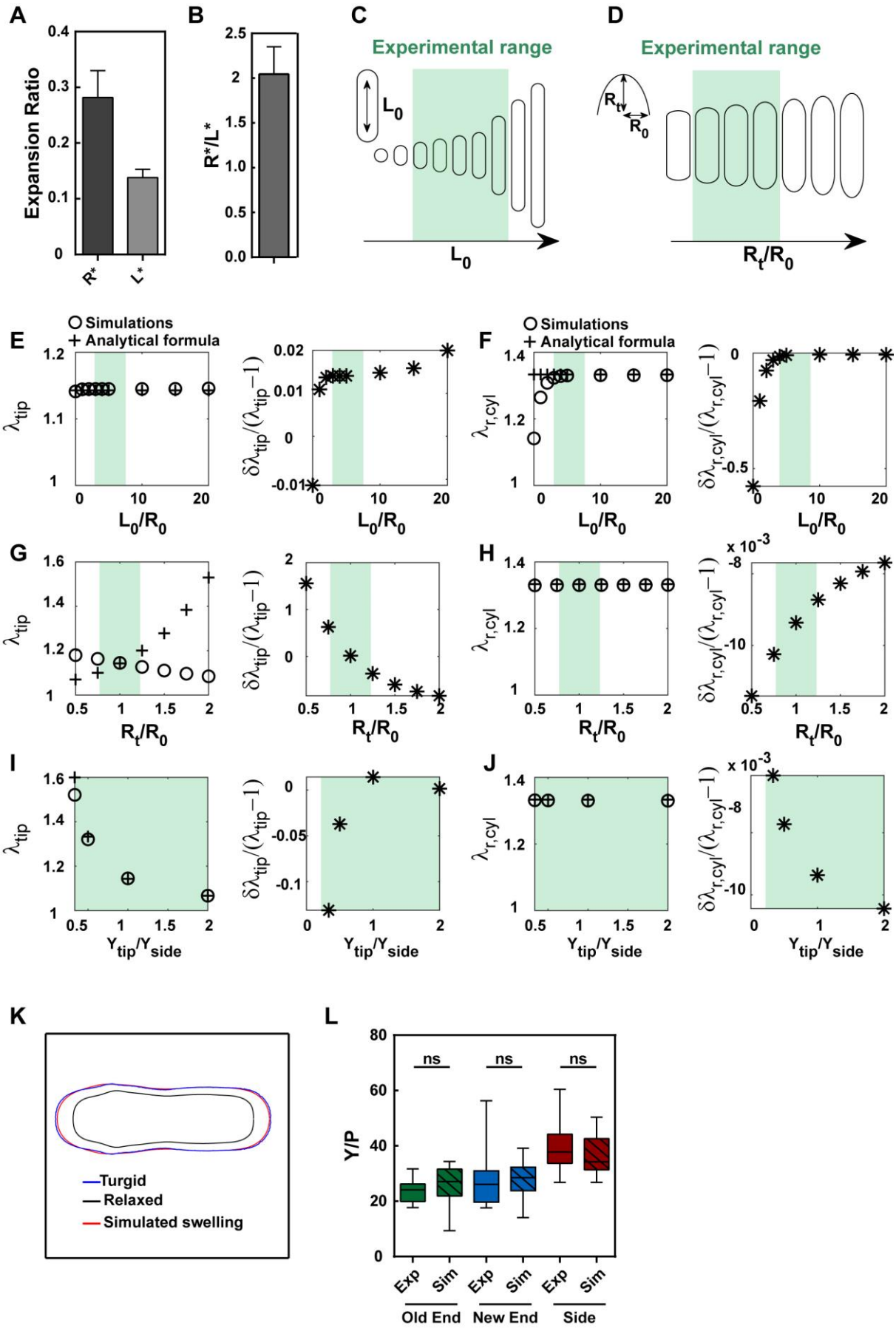
A
Expansion Ratio
R*
L*
B
R*/L*
C
Experimental range
L0
L0
D
Experimental range
Rt
R0
Rt/R0
E
Simulations
Analytical formula
λtip
L0/R0
δλtip/(λtip−1)
L0/R0
F
Simulations
Analytical formula
λr,cyl
L0/R0
δλr,cyl/(λr,cyl−1)
L0/R0
G
λtip
Rt/R0
δλtip/(λtip−1)
Rt/R0
H
λr,cyl
Rt/R0
x 10-3
δλr,cyl/(λr,cyl−1)
Rt/R0
I
λtip
Ytip/Yside
δλtip/(λtip−1)
Ytip/Yside
J
λr,cyl
Ytip/Yside
x 10-3
δλr,cyl/(λr,cyl−1)
Ytip/Yside
K
Turgid
Relaxed
Simulated swelling
L
Y/P
ns
ns
ns
Exp
Sim
Exp
Sim
Exp
Sim
Old End
New End
Side

Figure S1. Measurements and simulations assessing the validity of simple analytical formulae to compute local cell wall elastic moduli. (A) Relative expansion radius (measured as $(R_1-R_0)/R_0$) and relative expansion length (measured as $(L_1-L_0)/L_0$) of wt cells after laser ablation (n=99). **(B)** Ratio between the two expansion ratios calculated for each cell from **A** (n=99). **(C-J)** 3D simulations of radial or tip deformations defined as $\lambda_{r,cyl}= R_1/R_0$ and $\lambda_{tip} = Rc/Rc_0$, respectively, of inflated cells and comparisons with analytical formulae, for different cell geometries and wall mechanical patterns. In all graphs, the simulated data are shown with circles (o) and the analytical formulae with crosses (+). The relative differences between the analytical results and the simulated deformation, defined as $(\lambda_{simulation} - \lambda_{analytical})/(\lambda_{simulation}-1)$ are shown in the right part of each figure. The Poisson ratio is always set to 0 in the simulations and the cell wall thickness is h=0.2µm. The experimental range depicted by the green shade was assessed on ~100 cells covering all experimental conditions in this work (WT, mutants, different species) **(C)** The relaxed cylinder length (L_0) is varied from 0 to 40 µm (R_0=2 µm with hemispherical tips, Y_s/P=40). **(D)** R_t/R_0, the "ellipticity" of the relaxed tip, is varied from 0.5 to 2, the other parameters remaining constant (L_0=10 µm, R_0=2 µm, Y_s/P=40). **(E)** Tip deformation and **(F)** radial deformation (evaluated at the middle of the cylinder in simulations) as a function of L_0/R_0. **(G)** Tip deformation and **(H)** radial deformation (evaluated at the middle of the cylinder in simulations)) as a function of R_t/R_0. **(I-J)** The ratio between the Young modulus at the tip and at the side (Y_{tip}/Y_{side}) is varied from 0.3 to 2 the other parameters remaining constant (L_0=10 µm, R_0=2 µm hemispherical tip, Y_s/P=40). **(I)** Tip deformation. **(J)** Radial deformation (evaluated at the middle of the cylinder in simulations). **(K)** Simulation of cell swelling of a WT cell, obtained by using values of local surface moduli computed from analytical expressions reported in methods. In black and blue: measured relaxed and turgid cell boundary, in red: simulated turgid cell boundary. **(L)** Y/P values computed using analytical expressions (plain) or simulations (striped) at old ends, new ends and sides, for the same set of wt cells (n=27). Whisker plots represent median and full data set range.

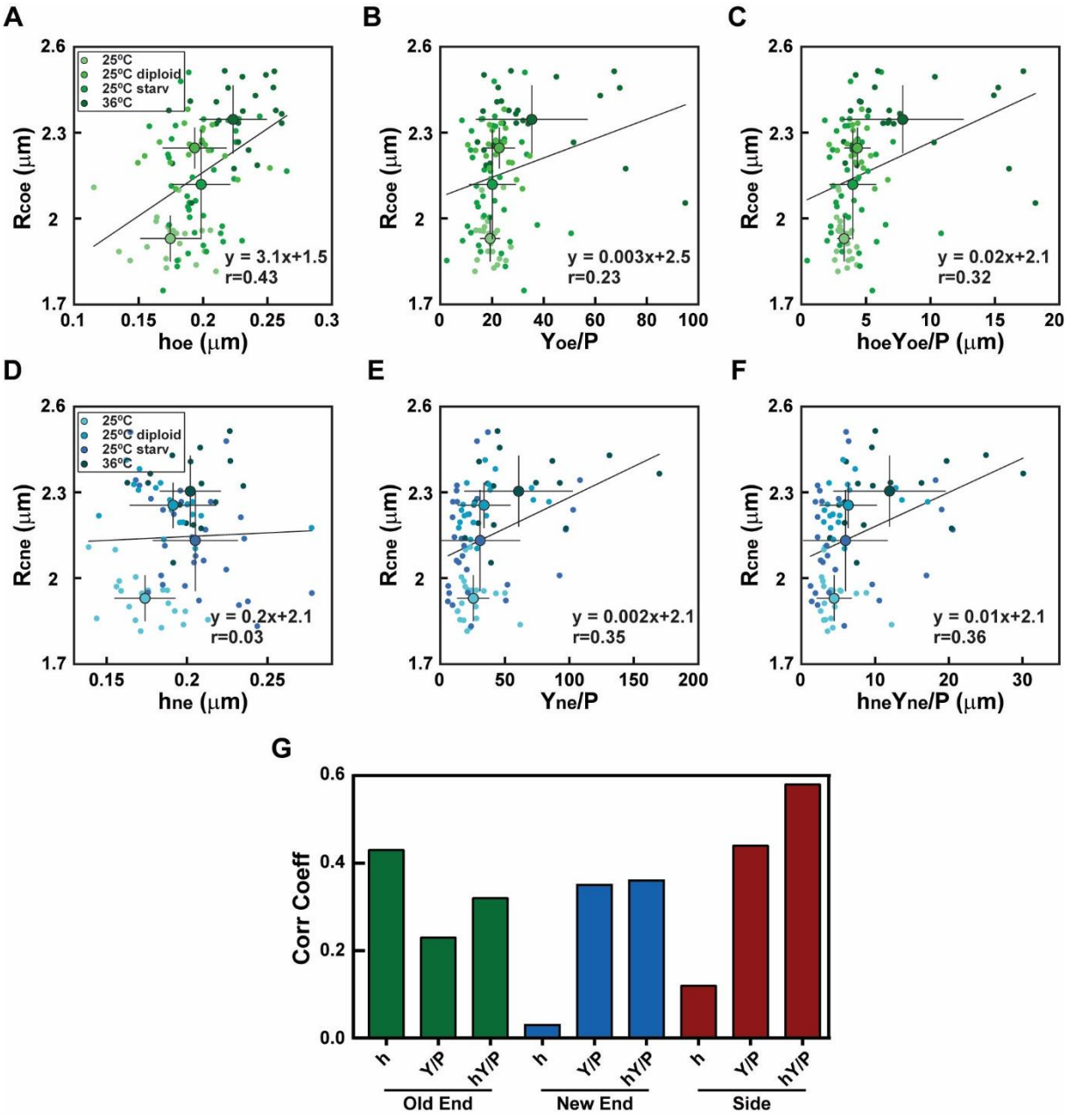
A
B
C
D
E
F
G
25°C
25°C diploid
25°C starv
36°C
Rcoe (μm)
hoe (μm)
y = 3.1x+1.5
r=0.43
Yoe/P
y = 0.003x+2.5
r=0.23
hoeYoe/P (μm)
y = 0.02x+2.1
r=0.32
Rcne (μm)
hne (μm)
y = 0.2x+2.1
r=0.03
Yne/P
y = 0.002x+2.1
r=0.35
hneYne/P (μm)
y = 0.01x+2.1
r=0.36
Corr Coeff
h
Y/P
hY/P
Old End
New End
Side

Figure S2. Local cell wall mechanical properties and local cell shape in fission yeast. (A-C) Radius of curvature at the old end (R_{oe}), plotted as a function of old end wall thickness (h_{oe}), old end bulk modulus divided by P (Y_{oe}/P) or surface modulus divided by P ($Y_{oe}h_{oe}/P$), in the same conditions as in **Fig. 1G** (for 25^0C n=21, 25^0C diploid n= 18, 25^0C starv n=39, 36^0C n=25). **(D-F)** Radius of curvature at the new end (R_{ne}), plotted as a function of new end wall thickness (h_{ne}), new end bulk modulus divided by P (Y_{ne}/P) or surface modulus divided by P ($Y_{ne}h_{ne}/P$), in the same conditions as in **Fig. 1G** (for 25^0C n=21, 25^0C diploid n= 19, 25^0C starv n=29, 36^0C n=17). For **A-F**, small dots correspond to single cells measurements, and the larger dot is the average. The line is a linear fit of single cell measurements. Error bars are standard deviations. **(G)** Pearson correlation coefficients, between the local radius and wall thickness (h), bulk modulus divided by pressure Y/P or surface modulus divided by pressure (hY/P), in different parts of the cell as indicated. Those values correspond to data presented in **A-F** and in **Fig. 1 H-J.**

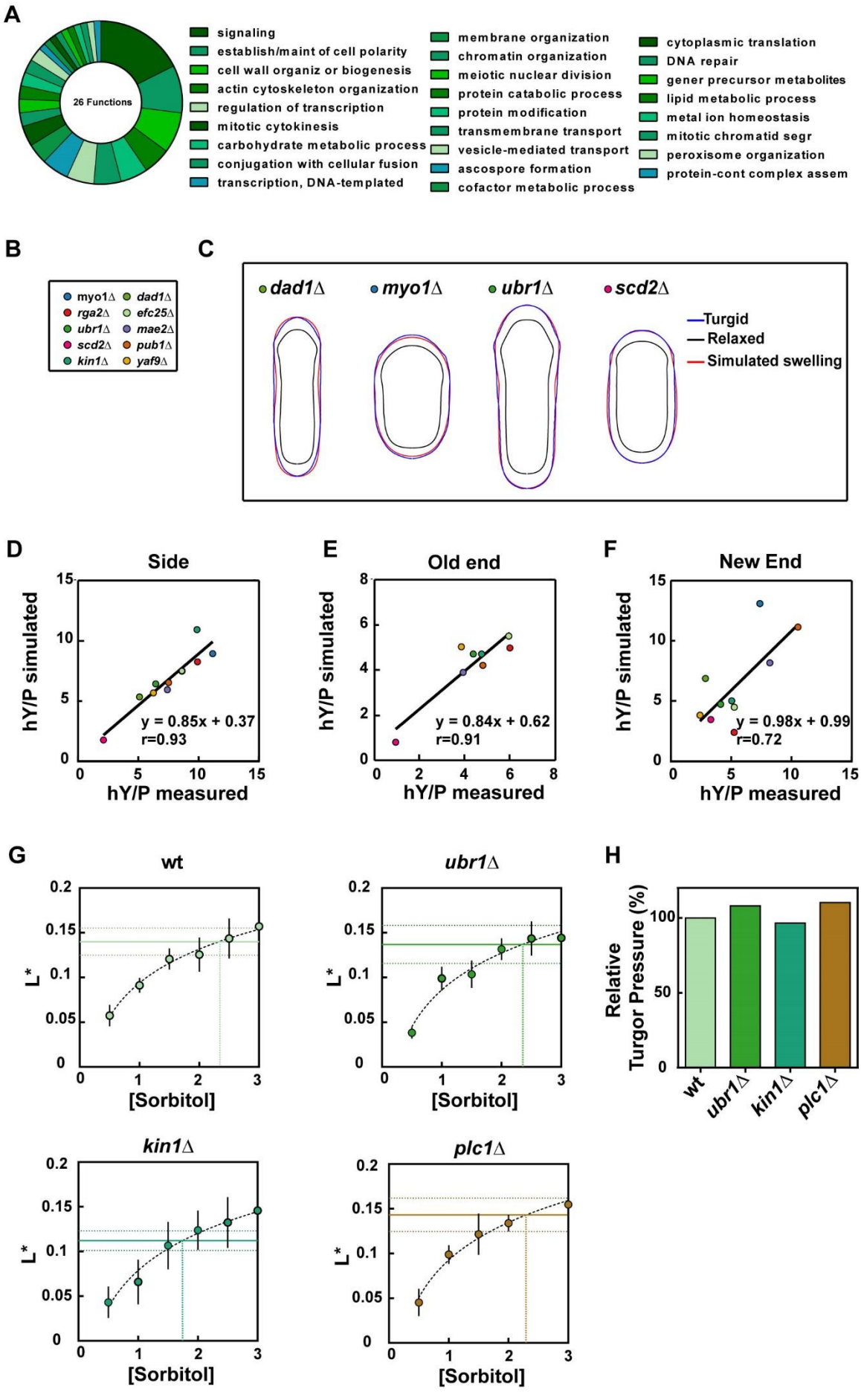
A
26 Functions
signaling
establish/maint of cell polarity
cell wall organiz or biogenesis
actin cytoskeleton organization
regulation of transcription
mitotic cytokinesis
carbohydrate metabolic process
conjugation with cellular fusion
transcription, DNA-templated
membrane organization
chromatin organization
meiotic nuclear division
protein catabolic process
protein modification
transmembrane transport
vesicle-mediated transport
ascospore formation
cofactor metabolic process
cytoplasmic translation
DNA repair
gener precursor metabolites
lipid metabolic process
metal ion homeostasis
mitotic chromatid segr
peroxisome organization
protein-cont complex assem
B
myo1Δ
dad1Δ
rga2Δ
efc25Δ
ubr1Δ
mae2Δ
scd2Δ
pub1Δ
kin1Δ
yaf9Δ
C
dad1Δ
myo1Δ
ubr1Δ
scd2Δ
Turgid
Relaxed
Simulated swelling
D
Side
hY/P simulated
hY/P measured
y = 0.85x + 0.37
r=0.93
E
Old end
hY/P simulated
hY/P measured
y = 0.84x + 0.62
r=0.91
F
New End
hY/P simulated
hY/P measured
y = 0.98x + 0.99
r=0.72
G
wt
ubr1Δ
kin1Δ
plc1Δ
L*
[Sorbitol]
H
Relative Turgor Pressure (%)
wt
ubr1Δ
kin1Δ
plc1Δ

Figure S3. Classification of diameter defective mutants, validations of the method used to compute elastic moduli by 3D simulations, and variations in turgor values between mutants. (A) Pie chart of Gene Ontology classification of the mutants used in the screen presented in **Fig. 2**. The list starts with the most abundant and follows in a clockwise direction. **(B)** Legend for the conditions or mutants used in **B-F.** **(C)** Simulations of cell swelling of representative mutant cells from the screen results of Fig 2F-2H, obtained by using values of local surface moduli computed from analytical expressions reported in methods. In black and blue: measured relaxed and turgid cell boundary, in red: simulated turgid cell boundary. **(D-F)** Plots of simulation values of the surface moduli of 10 cells of different mutants, obtained from best fits of simulated swelling, plotted as a function of surface moduli of the same cells computed from analytical expressions reported in methods: **(D)** cell sides, **(E)** old ends, and **(F)** new ends. Bold lines represent linear fits, and r values correspond to Pearson correlation coefficients. **(G)** Relative expansion length of cells from the indicated strains, grown in YE5S and treated with different sorbitol concentrations in YE5S. Dots represent an average of a treated population (n>10). L* is measured as $(L_1-L_{osm})/L_{osm}$) where L_{osm} is the length after osmotic treatment. The horizontal plain line represents an average of the relative expansion length obtained in the same strain using laser ablation ($L_{osm}=L_0$), horizontal dotted lines indicate the corresponding standard deviation. The vertical line starts from the intersection between averaged L* and a logarithmic fit, and ends in the intersection with the *x* axis. **(H)** Turgor pressure of indicated strains, relative to wt turgor pressure, calculated as $(P_{strain}/P_{wt})*100$.

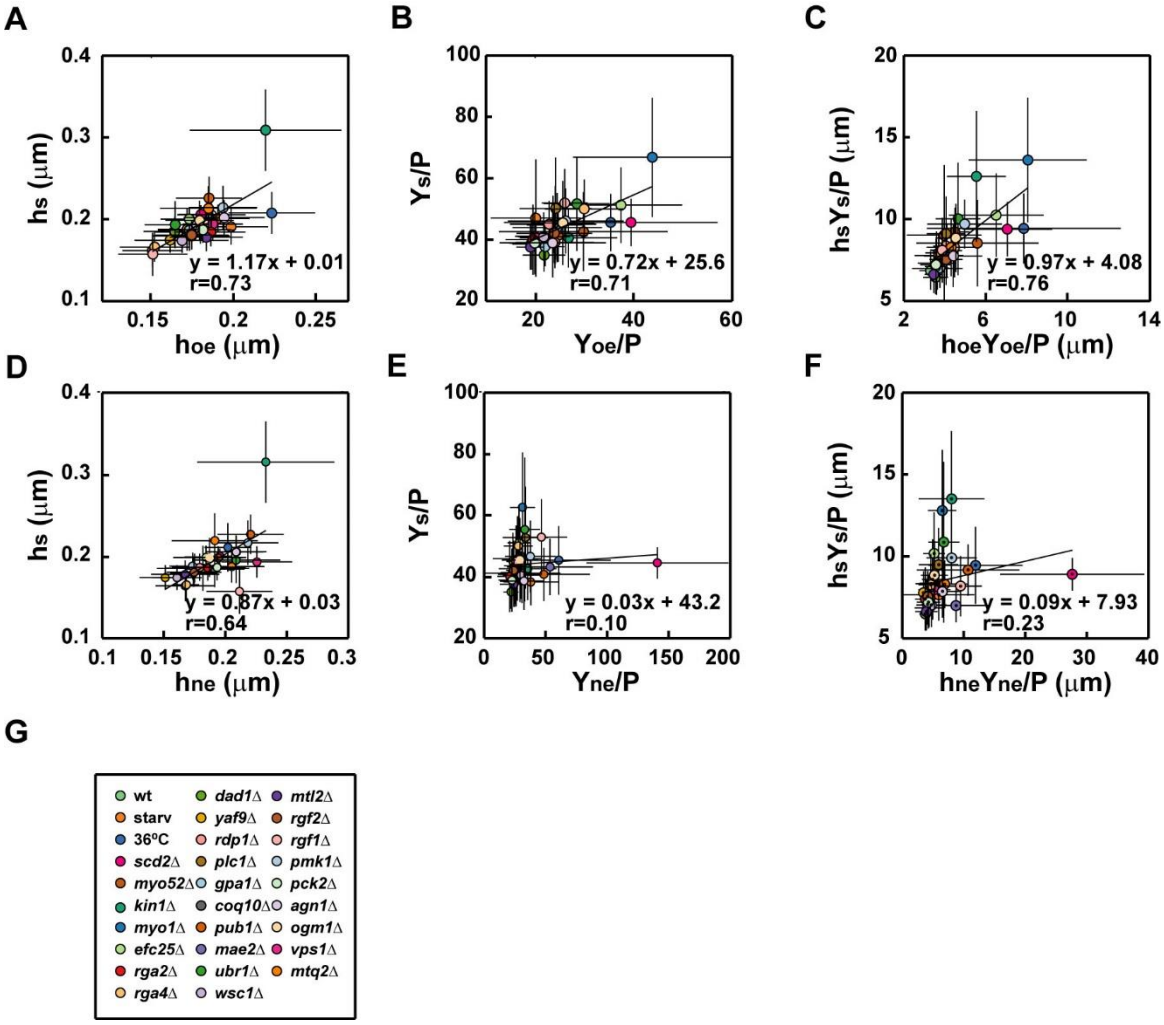
A
hs (μm)
hoe (μm)
y = 1.17x + 0.01
r=0.73
B
Ys/P
Yoe/P
y = 0.72x + 25.6
r=0.71
C
hsYs/P (μm)
hoeYoe/P (μm)
y = 0.97x + 4.08
r=0.76
D
hs (μm)
hne (μm)
y = 0.87x + 0.03
r=0.64
E
Ys/P
Yne/P
y = 0.03x + 43.2
r=0.10
F
hsYs/P (μm)
hneYne/P (μm)
y = 0.09x + 7.93
r=0.23
G
wt
starv
36ºC
scd2Δ
myo52Δ
kin1Δ
myo1Δ
efc25Δ
rga2Δ
rga4Δ
dad1Δ
yaf9Δ
rdp1Δ
plc1Δ
gpa1Δ
coq10Δ
pub1Δ
mae2Δ
ubr1Δ
wsc1Δ
mtl2Δ
rgf2Δ
rgf1Δ
pmk1Δ
pck2Δ
agn1Δ
ogm1Δ
vps1Δ
mtq2Δ

Figure S4. Correlations between tips and lateral cell wall mechanics. (A-C) CW thickness, bulk elastic modulus divided by pressure, and surface modulus divided by pressure on cell sides plotted as a function of those at old ends. **(D-F)** CW thickness, bulk elastic modulus divided by pressure, and surface modulus divided by pressure on cell sides plotted as a function of those at new ends. **(G)** Legend for the conditions or mutants used in **A-F.** r values are Pearson correlation coefficients. Error bars are standard deviations.

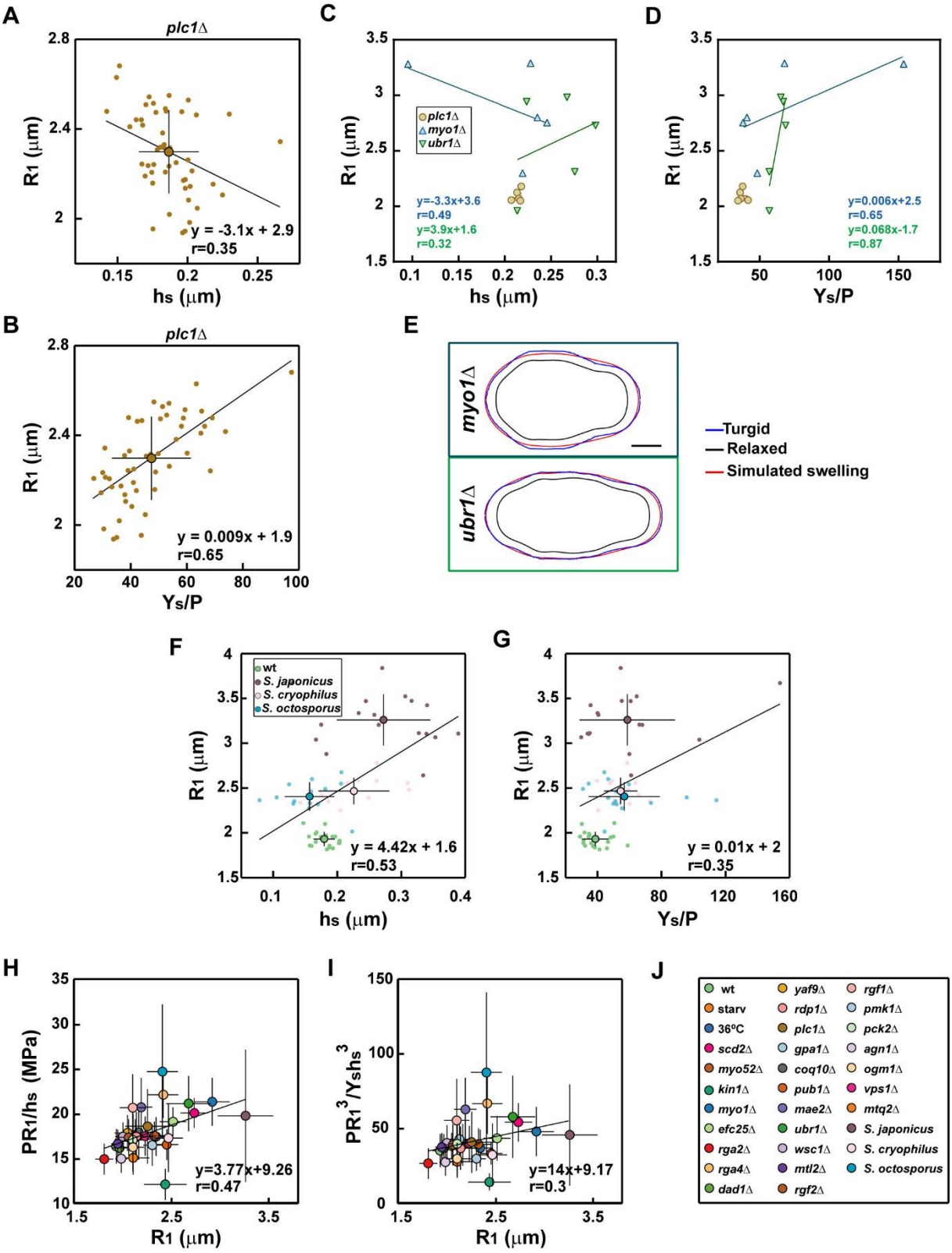
A
plc1Δ
R1 (μm)
hs (μm)
y = -3.1x + 2.9
r=0.35
B
plc1Δ
R1 (μm)
Ys/P
y = 0.009x + 1.9
r=0.65
C
plc1Δ
myo1Δ
ubr1Δ
R1 (μm)
hs (μm)
y=-3.3x+3.6
r=0.49
y=3.9x+1.6
r=0.32
D
R1 (μm)
Ys/P
y=0.006x+2.5
r=0.65
y=0.068x-1.7
r=0.87
E
myo1Δ
ubr1Δ
Turgid
Relaxed
Simulated swelling
F
wt
S. japonicus
S. cryophilus
S. octosporus
R1 (μm)
hs (μm)
y = 4.42x + 1.6
r=0.53
G
R1 (μm)
Ys/P
y = 0.01x + 2
r=0.35
H
PR1/hs (MPa)
R1 (μm)
y=3.77x+9.26
r=0.47
I
PR1^3/Yshs^3
R1 (μm)
y=14x+9.17
r=0.3
J
wt
starv
36ºC
scd2Δ
myo52Δ
kin1Δ
myo1Δ
efc25Δ
rga2Δ
rga4Δ
dad1Δ
yaf9Δ
rdp1Δ
plc1Δ
gpa1Δ
coq10Δ
pub1Δ
mae2Δ
ubr1Δ
wsc1Δ
mtl2Δ
rgf2Δ
rgf1Δ
pmk1Δ
pck2Δ
agn1Δ
ogm1Δ
vps1Δ
mtq2Δ
S. japonicus
S. cryophilus
S. octosporus

Figure S5. Evolution of key mechanical values in the CW as a function of cell radius.
(A-B) Cell radius (R_1) plotted as a function of side wall thickness (h_s, **A**) and bulk modulus divided by P (Y_s/P, **B**) for individual cells within a population of *plc1Δ* mutant (n=50). **(C-D)** Local radius (R_1), plotted as a function of the corresponding side wall thickness (h_s, **C**) and bulk modulus divided by P (Y_s/P, **D**) in 5 different parts along the side of the same cell, for the cells represented in **Fig. 3B**. **(E)** Simulation of cell swelling in skittle cells of the indicated strains, obtained by using values of local surface moduli estimated experimentally as in **C-D** and **Fig. 3B**. In black and blue: measured relaxed and turgid cell boundary, in red: simulated turgid cell boundary. **(F)** Cell radius (R_1) plotted as a function of side wall thickness (h_s), **(G)** and side bulk modulus divided by P (Y_s/P) in *S. pombe* (n=21), S. *japonicus* (n=17), *S. octosporus* (n=14), and *S. cryophylus* (n=12). **(H)** Elastic stress in the cell wall (PR_1/h_s) plotted as a function of cell radii and **(I)** energy corresponding to cell wall bending normalized to the energy of pressure ($PR^3_1/h^3_sY_s$) plotted as a function of cell radii. **(J)** Legend for the conditions or mutants used in **H-I.** Where present, small dots are single cells measurements, and the big dot is the average. In A-D and F-G the line is a linear fit of single cell measurements. In H-I the line is a linear fit of averages. r values are Pearson correlation coefficients. Error bars represent standard deviations. Scale bar, 2μm.

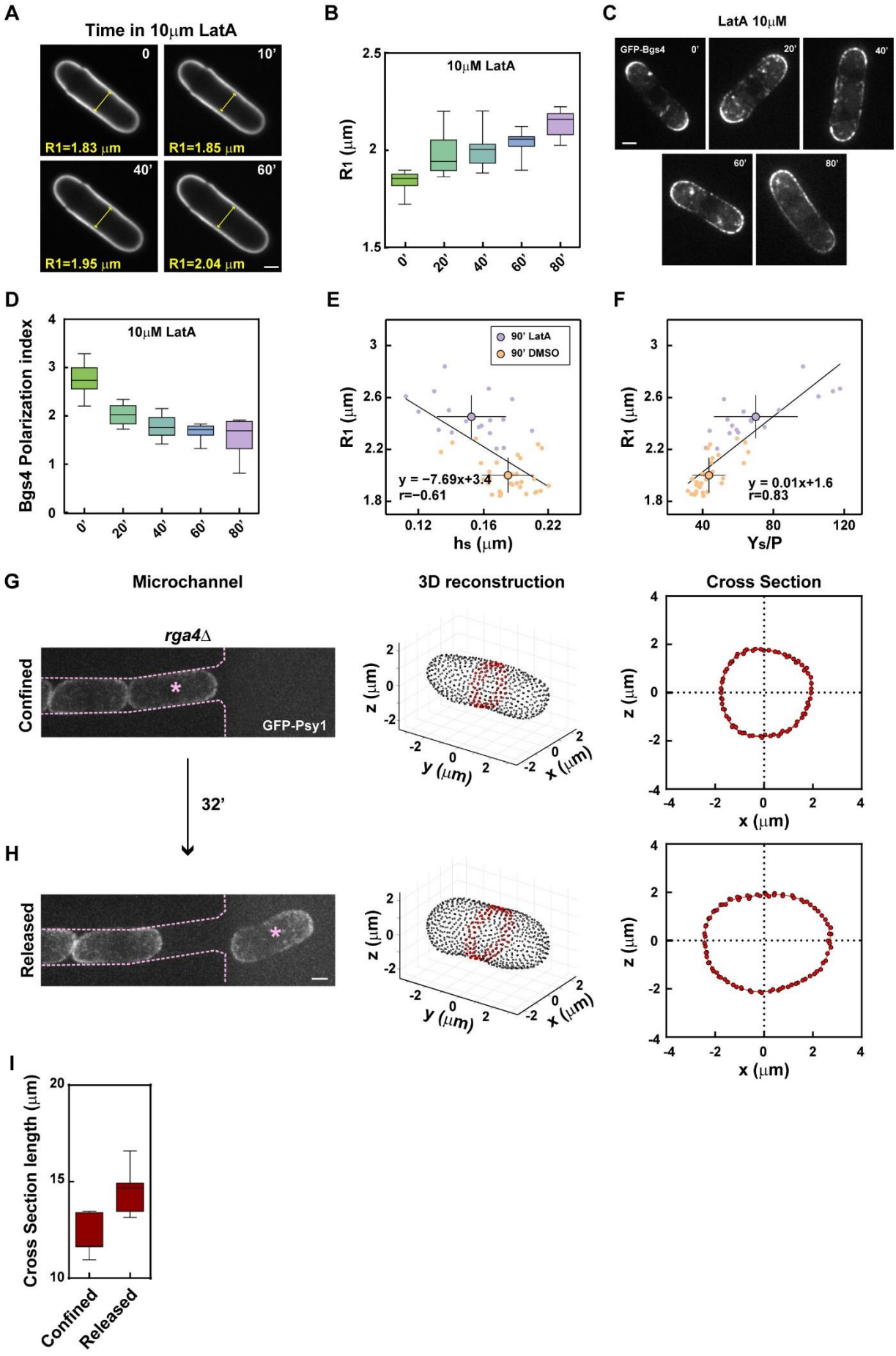
A
Time in 10μm LatA
0
10'
R1=1.83 μm
R1=1.85 μm
40'
60'
R1=1.95 μm
R1=2.04 μm
B
10μM LatA
R1 (μm)
2.5
2
1.5
0'
20'
40'
60'
80'
C
LatA 10μM
GFP-Bgs4
0'
20'
40'
60'
80'
D
10μM LatA
Bgs4 Polarization index
4
3
2
1
0
0'
20'
40'
60'
80'
E
90' LatA
90' DMSO
R1 (μm)
3
2.6
2.2
1.8
y = −7.69x+3.4
r=−0.61
0.12
0.16
0.22
hs (μm)
F
R1 (μm)
3
2.6
2.2
1.8
y = 0.01x+1.6
r=0.83
40
80
120
Ys/P
G
Microchannel
rga4Δ
Confined
GFP-Psy1
32'
H
Released
3D reconstruction
Cross Section
z (μm)
y (μm)
x (μm)
I
Cross Section length (μm)
20
15
10
Confined
Released

Figure S6. Evolution of cell diameter and CW mechanics upon dynamic shape manipulations. (A) Time-lapse of shape changes in a wt cell after treatment with 10μM Latrunculin A. The cell is labeled with lectin *Gs*-Alexafluor647. **(B)** Quantification of cell radius (R_1) evolution as a function of time. **(C)** Typical GFP-Bgs4 localization after treatment with 10μM Latrunculin A. **(D)** Quantification of GFP-Bgs4 polarity index (tip signal divided by full cell contour signal) in cells treated as in **A**. **(E)** Mean cell radius (R_1), plotted as a function of side wall thickness (h_s), and **(F)** side bulk modulus (Y_s/P) in wt cells treated for 1.5 hr with DMSO (n=30) or 10μM LatrunculinA (n=18). Small dots are single cells measurements, and larger dots are averages. Lines are linear fits on single cell measurements. r values are Pearson correlation coefficients. **(G-H)** (Left) Maximum projection of 15 slices of *rga4Δ* cells expressing GFP-psy1 and grown inside a microchannel. The cell indicated by the asterisk is confined in (G) and released in (H). Note the rapid change in cell diameter. 3D reconstruction (Center) and cross section (Right) of the cell marked with an asterisk on the left before and after exiting the microchannel. **(I)** Cell perimeter of *rga4Δ* cells grown in microchannels before and after release. (n=7).

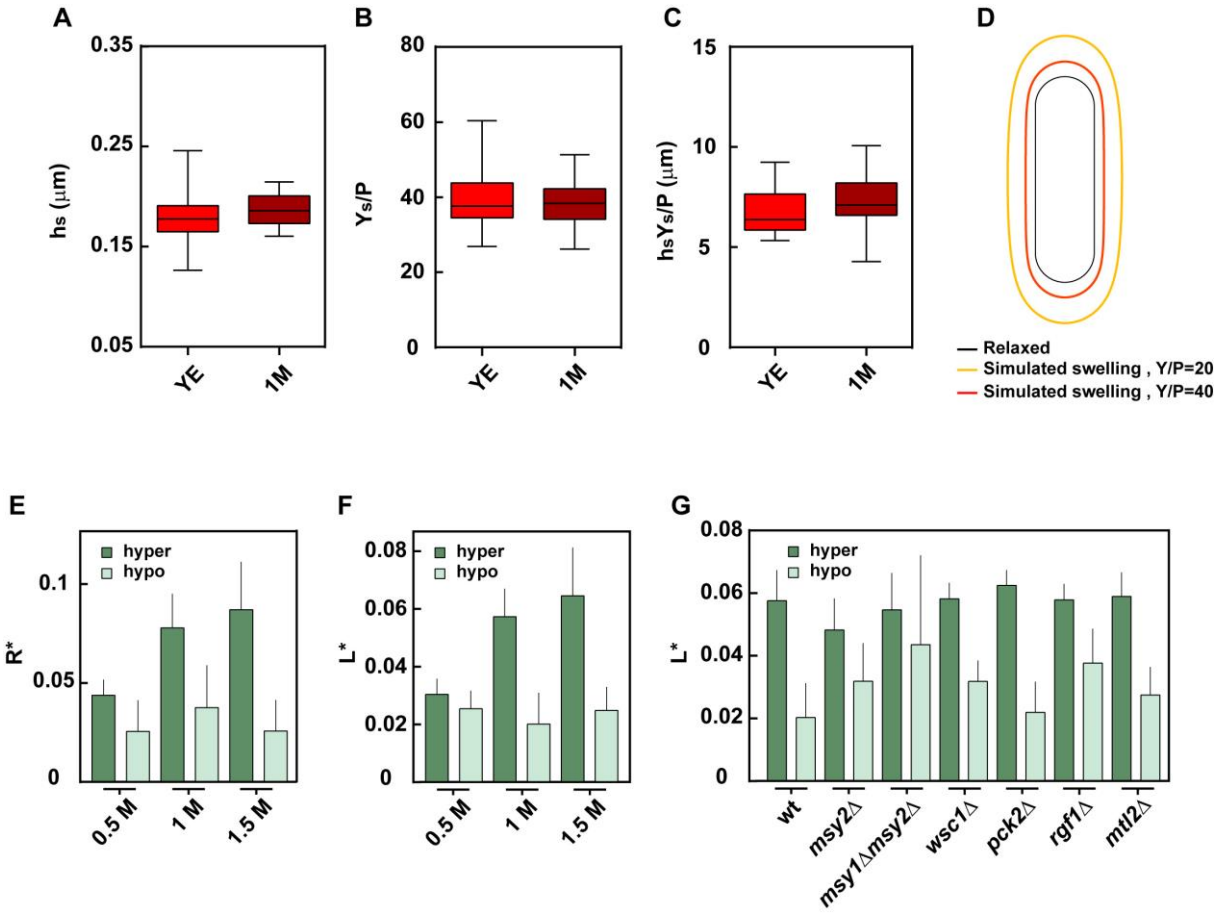
A
hs (μm)
0.35
0.25
0.15
0.05
YE
1M
B
Ys/P
80
60
40
20
0
YE
1M
C
hsYs/P (μm)
15
10
5
0
YE
1M
D
Relaxed
Simulated swelling , Y/P=20
Simulated swelling , Y/P=40
E
R*
hyper
hypo
0.1
0.05
0
0.5 M
1 M
1.5 M
F
L*
hyper
hypo
0.08
0.06
0.04
0.02
0
0.5 M
1 M
1.5 M
G
L*
hyper
hypo
0.08
0.06
0.04
0.02
0
wt
msy2Δ
msy1Δmsy2Δ
wsc1Δ
pck2Δ
rgf1Δ
mtl2Δ

Figure S7. Quantifications of cell shape and CW mechanics in response to hyper- and hypo-osmotic treatments. (A-C) Lateral CW thickness (A), bulk modulus (B), and surface modulus (C) in control wt cells and in cells adapted for 1h in 1M sorbitol. **(D)** Swelling of a relaxed cell (L_0=10 μm, R_0=2 μm, hemispherical tip) shown with the inner dashed contour, with different pressure, to support the existence of strain-stiffening effects in experiments. At a pressure such that $Y_s/P=40$ (red line), the cell is cylindrical, whereas at a pressure such that $Y_s/P=20$ (yellow line), the cell starts to be slightly ovalized. **(E)** Relative expansion/contraction radius measured as $(R_{0.5M}-R_{1M})/R_{0.5M}$, $(R_{1M}-R_{2M})/R_{1M}$ and $(R_{1.5M}-R_{3M})/R_{1.5M}$ for hyper- (dark green), or as $(R_{YE}-R_{0.5M})/R_{0.5M}$, $(R_{YE}-R_{1M})/R_{1M}$ and $(R_{YE}-R_{1.5M})/R_{1.5M}$ for hypo- (light green) osmotic treatment after adaptation to 0.5M , 1M and 1.5M sorbitol, respectively (0.5M, n=8 cells; 1M, n=10 cells; 1.5M n=14 cells). **(F)** Relative expansion/ contraction length measured as for radii and in the same cells as in D. **(G)** Relative expansion/contraction lengths measured as $(L_{1M}-L_{2M})/L_{1M}$ for hyper (dark green), or as $(L_{YE}- L_{1M})/L_{1M}$ for hypo (light green) in cells treated as in **Fig. 4 H**, in the indicated strains (n=10 in each conditions). Error bars are standard deviations.